Nonlin. Processes Geophys., 15, 233–244, 2008
www.nonlin-processes-geophys.net/15/233/2008/

Nonlinear Processes in Geophysics

Generation of weakly nonlinear nonhydrostatic internal tides over large topography: a multi-modal approach

R. Maugé[1] **and T. Gerkema**[2]

[1]Laboratoire de Physique des Océans, Université de Bretagne Occidentale, 6 avenue Le Gorgeu, 29238 Brest, France
[2]Royal Netherlands Institute for Sea Research, P.O. Box 59, 1790 AB Den Burg, The Netherlands

Received: 11 June 2007 – Revised: 13 November 2007 – Accepted: 15 November 2007 – Published: 7 March 2008

Abstract. A set of evolution equations is derived for the modal coefficients in a weakly nonlinear nonhydrostatic internal-tide generation problem. The equations allow for the presence of large-amplitude topography, e.g. a continental slope, which is formally assumed to have a length scale much larger than that of the internal tide. However, comparison with results from more sophisticated numerical models show that this restriction can in practice be relaxed. It is shown that a topographically induced coupling between modes occurs that is distinct from nonlinear coupling. Nonlinear effects include the generation of higher harmonics by reflection from boundaries, i.e. steeper tidal beams at frequencies that are multiples of the basic tidal frequency. With a seasonal thermocline included, the model is capable of reproducing the phenomenon of local generation of internal solitary waves by a tidal beam impinging on the seasonal thermocline.

1 Introduction

In the central Bay of Biscay, internal solitary waves (ISWs) have been observed that are generated by an upward propagating internal tidal beam as it meets the seasonal thermocline (New and Pingree, 1990, 1992; New and Da Silva, 2002). This local generation of ISWs was studied theoretically and numerically by Gerkema (2001), who showed that it involves two steps. First, the impinging beam generates a depression of the thermocline – an essentially linear process. This depression then propagates away, steepens, and splits up into solitary waves; in these later stages, both nonlinear and nonhydrostatic effects are essential. It was moreover shown that this local generation occurs only if the seasonal thermocline is of moderate strength.

Correspondence to: R. Maugé
(rudy.mauge@hocer.com)

Although the essential ingredients of the process thus seem to have been clarified, we should emphasize the idealized setting of the study by Gerkema (2001), as it involves a schematic stratification (a mixed layer, an interface representing the thermocline, and a layer of constant stratification beneath it), and infinitesimal topography. In reality, of course, the stratification varies throughout the water column, and, more importantly, the internal tidal beams are generated over the continental slope, in other words, over large-amplitude topography. In principle, all these elements could be included in fully nonlinear nonhydrostatic numerical models, such as employed in other contexts by Lamb (1994), Vlasenko and Morozov (1993), or the MIT-model (e.g. Khatiwala, 2003). These models are however computationally demanding, and technical problems like numerical instabilities may occur when one attempts to include a seasonal thermocline. By contrast, weakly nonhydrostatic models – such us the Korteweg-de Vries equation (see, e.g., Helfrich and Melville, 2006) or extensions thereof involving internal-tide generation – can be solved numerically in an efficient way. However, they are based on separation of variables and decomposition into vertical modes, and hence require small (infinitesimal, strictly) topography.

In this paper we present a way to circumvent this problem: we apply vertical modes despite the presence of large-amplitude topography. We are able to do so by assuming that the *horizontal* scale of topography is much larger than the (horizontal) wavelength of the internal tide. In a perturbative approach, we thus find at the lowest order that topography enters the problem merely in a parametric way, whereas at the next order, interaction (i.e. exchange of energy) between the modes occurs over topography, even if nonlinear terms were neglected. At this same order, the other supposedly weak effects appear (nonlinearity, nonhydrostaticity).

It may seem as if the assumption on the lengthscale of topography poses a severe restriction on the range of applications of this model; indeed, in the ocean it is typically of the

Published by Copernicus Publications on behalf of the European Geosciences Union and the American Geophysical Union.

same order as the wavelength of the internal tide, instead of being much larger. However, it is not unusual to find in studies using WKB-type approximations that the formal restriction can in practice be relaxed, even to the point where the "small parameter" comes close to one (examples are given in Bender and Orszag, 1978). This will be confirmed here by comparisons with fully numerical models involving no such restriction (Sect. 3b). The resulting set of model equations allows us to study, in a fairly realistic setting, the generation of higher harmonics (Sect. 4a), and the local generation of ISWs (Sect. 4b). The latter process has not been previously modelled in such a realistic setting.

2 Derivation of a weakly nonlinear nonhydrostatic model

In this section we outline the derivation of the model equations. We consider uniformity in one of the horizontal directions, i.e. $\partial/\partial y$=0. On the f-plane, the momentum equations then read

$$u_t + uu_x + wu_z - fv = -p_x \tag{1}$$

$$v_t + uv_x + wv_z + fu = 0 \tag{2}$$

$$w_t + uw_x + ww_z = -p_z - \rho g/\rho_* \tag{3}$$

where u, v, w are the velocity components in the x, y, z directions, ρ density, ρ_* a constant reference value of density, and p pressure (divided by ρ_*). Here the Boussinesq approximation is applied. These equations are to be supplemented by the equations expressing mass and energy conservation, which under the assumptions of incompressibility and adiabatic motion become, respectively,

$$u_x + w_z = 0 \tag{4}$$

$$\rho_t + u\rho_x + w\rho_z = 0\,. \tag{5}$$

The momentum Eq. (1) and (3) can be combined into an equation for the streamfunction ψ, with $u{=}\psi_z$ and $w{=}-\psi_x$,

$$\nabla^2\psi_t + J(\nabla^2\psi, \psi) - fv_z + b_x = 0\,, \tag{6}$$

where $b{=}-g(\rho{-}\rho_0)/\rho_*$ denotes buoyancy, $\rho_0(z)$ being the static density field. The Jacobian J is defined as $J(p, q){=}p_xq_z{-}p_zq_x$. In terms of ψ and b, (2) and (5) become

$$v_t + J(v, \psi) + f\psi_z = 0 \tag{7}$$

$$b_t + J(b, \psi) - N^2\psi_x = 0\,, \tag{8}$$

where $N^2{=}-(g/\rho_*)d\rho_0/dz$ is the buoyancy frequency, a measure of the background stratification. The set (6)–(8) forms the starting point for further analysis. As yet, the equations describe the full, i.e. barotropic plus baroclinic, fields.

We impose a barotropic forcing in the simple form of a time-oscillating but horizontally uniform flux, by using the following boundary conditions:

$$\begin{aligned} &\psi = 0 \ \text{ at } z = 0 \ \text{ (surface)} \\ &\psi = Q\sin(\omega t) \ \text{ at } z = h(x) \ \text{ (bottom)}, \end{aligned} \tag{9}$$

where Q is the amplitude of the barotropic flux, and ω the tidal frequency. Following Garrett and Gerkema (2007), we make the transformation

$$\psi = \Psi_0 + \psi'\,, \quad \text{with } \ \Psi_0 = \frac{z}{h(x)}\,Q\sin(\omega t)\,.$$

With this, (6)–(8) become

$$\nabla^2\psi'_t + U\nabla^2\psi'_x + J(\nabla^2\psi', \psi') - fv'_z + b_x = S_1 \tag{10}$$

$$v'_t + Uv'_x + J(v', \psi') + f\psi'_z = S_2 \tag{11}$$

$$b_t + Ub_x + J(b, \psi') - N^2\psi'_x = -N^2W + S_3, \tag{12}$$

where we introduced $U{=}\Psi_{0,z}$ and $W{=}-\Psi_{0,x}$, which we will loosely refer to as "barotropic", the primed field ψ' being "baroclinic". This interpretation is correct in the absence of topography, but over the slope ψ' actually contains a nonhydrostatic correction to the barotropic field, as pointed out by Garrett and Gerkema (2007). The transverse velocity v is also split, as $v{=}V{+}v'$, with $V_t{=}-fU$. The buoyancy field b, on the other hand, is retained in its full form. On the right-hand sides, we find the terms $S_{1,2,3}$, which stand for

$$S_1 = W_{xt} - W\nabla^2\psi'_z + (U + \psi'_z)W_{xx} - (W - \psi'_x)U_{xx} \tag{13}$$

$$S_2 = -Wv'_z - (U + \psi'_z)V_x \tag{14}$$

$$S_3 = -Wb_z\,. \tag{15}$$

Note that each term contains a barotropic field. In later sections, we show that $S_{1,2,3}$ can be neglected under the assumptions that we will adopt. The barotropic effects explicitly included in (10)–(12), which cannot be neglected, are the advective terms $U(\cdot)_x$, and, most important of all, the body-force term on the right-hand side of (12): $-N^2W$; this is the generator of internal tides.

The boundary conditions (9) are now to be replaced by

$$\begin{aligned} &\psi' = 0 \ \text{ at } z = 0 \ \text{ (surface);} \\ &\psi' = 0 \ \text{ at } z = h(x) \ \text{ (bottom).} \end{aligned} \tag{16}$$

Hereafter we drop the primes.

2.1 Scaling and first approximations

We cast the equations in dimensionless form by introducing the following scalings:

$$[t] = \omega^{-1}\,; \ \ [x] = L\,; \ \ [z, h] = H;$$

$$[U] = \frac{Q}{H}\,; \quad [W] = \frac{Q}{L};$$

$$[\psi] = Q; \ \ [v] = \frac{fQ}{\omega H}; \ \ [b] = \frac{Q\omega L}{H^2}.$$

Here H is a typical deep-ocean depth, and L the lengthscale of the internal tide. (The scale of b follows from assuming a primary balance between ψ_{zzt} and b_x in (10).) With this, (10)–(12) become

$$\nabla^2\psi_t + \gamma U\nabla^2\psi_x + \gamma J(\nabla^2\psi, \psi) - \mu v_z + b_x = S_1 \quad (17)$$

$$v_t + \gamma U v_x + \gamma J(v, \psi) + \psi_z = S_2 \quad (18)$$

$$b_t + \gamma U b_x + \gamma J(b, \psi) - N_s^2\psi_x = -N_s^2 W + S_3\,, \quad (19)$$

where we use the same symbols, for convenience, which now denote dimensionless quantities. To avoid confusion, however, we have introduced a new symbol $N_s{=}HN/(L\omega)$. The operator ∇ now stands for

$$\nabla^2 = \delta\frac{\partial^2}{\partial x^2} + \frac{\partial^2}{\partial z^2}\,.$$

Three parameters appear, being a measure of the strength of nonlinearity, nonhydrostaticity, and Coriolis effects, respectively:

$$\gamma = \frac{Q}{HL\omega}\,; \quad \delta = \left(\frac{H}{L}\right)^2; \quad \mu = \left(\frac{f}{\omega}\right)^2. \quad (20)$$

In line with KdV-type equations, we will assume nonlinear and nonhydrostatic effects to be weak, and of the same order of magnitude:

$$\gamma = O(\delta) \ll 1\,.$$

Hereafter we will neglect all terms of order $\gamma\delta$; in the nonlinear terms on the left-hand side of (17) we can thus replace $\nabla^2\psi$ with ψ_{zz}, since the other term is of order $\gamma\delta$. At this stage, we do not make any assumption on μ.

2.2 Slowly varying topography

The crux of this derivation lies in the assumption that the topography varies slowly with respect to the horizontal scale of the internal tide. Thus, we introduce a "slow" horizontal coordinate $X{=}\epsilon x$, with

$$\epsilon = \frac{\text{internal-tide length scale}}{\text{topographic length scale}} \ll 1\,. \quad (21)$$

This coordinate X is used as an independent variable in its own right, along with x. Specifically, it acts as the independent variable in $h(X)$, and in the barotropic fields U and W, whose only horizontal dependence is on X. Other fields, like ψ, depend on both "slow" and "normal" horizontal coordinates (X, x, respectively). Correspondingly, derivatives in x now take the form

$$\frac{\partial}{\partial x} \to \frac{\partial}{\partial x} + \epsilon\frac{\partial}{\partial X}\,.$$

We will furthermore assume that ϵ is of the same order as γ (and δ); thus, in line with earlier assumptions, we can neglect terms of order ϵ^2, or smaller.

It is now clear that the expressions $S_{1,2,3}$, given in unscaled form in (13)–(15), can be neglected in their entirety. The first term on the right-hand side of (13) contains W_x, which equals, in terms of the slow coordinate, $-\epsilon^2\Psi_{0,XX}$, and hence is negligible. All the remaining terms in (13)–(15) are nonlinear terms and thus have the small parameter γ. Moreover, each of them contains a derivative in X (via W, U_{xx}, or V_x), which produces an additional factor ϵ. All in all, they are of order $O(\gamma\epsilon)$, or smaller, and hence negligible.

Moreover, in the nonlinear and nonhydrostatic terms on the left-hand sides of (17)–(19), which are by themselves already of order γ, derivatives $\epsilon\partial/\partial X$ can be ignored since they produce terms of order $\gamma\epsilon$. The resulting equations thus become

$$\delta\psi_{xxt} + \psi_{zzt} + \gamma U\psi_{zzx} + \gamma J(\psi_{zz}, \psi) - \mu v_z + b_x + \epsilon b_X = 0 \quad (22)$$

$$v_t + \gamma U v_x + \gamma J(v, \psi) + \psi_z = 0 \quad (23)$$

$$b_t + \gamma U b_x + \gamma J(b, \psi) - N_s^2(\psi_x + \epsilon\psi_X) = -\epsilon N_s^2\frac{z}{h^2}h_X\sin t\,, \quad (24)$$

where J stands for $J(p, q){=}p_xq_z{-}p_zq_x$ and involves no derivative in X, for the abovementioned reason.

2.3 Transformation to terrain following coordinates

We now transform the vertical such that the bottom becomes purely horizontal in the new coordinate system:

$$\eta = -\frac{z}{h(X)}\,.$$

So, while the surface remains at $\eta{=}0$, the bottom now lies at $\eta{=}{-}1$. Correspondingly, we introduce new variables, for example

$$\Psi(t, x, X, \eta(X, z)) = \psi(t, x, X, z)\,,$$

and v and b are similarly replaced by the new variables Λ and B. In replacing the derivatives in X and z, we have to apply the chain rule, so

$$\psi_X = \Psi_X + \beta\Psi_\eta\,; \quad \psi_z = \alpha\Psi_\eta\,,$$

where

$$\alpha = \eta_z = -\frac{1}{h}\,; \quad \beta = \eta_X = -\frac{\eta}{h}\,h_X\,.$$

Note that the $N_s(z)$ now depends on both horizontal and vertical coordinates, since in the new coordinates it becomes $N_s(-\eta h(X))$. With this transformation, (22)–(24) become

$$\delta\Psi_{xxt} + \alpha^2(\Psi_{\eta\eta t} + \gamma U\Psi_{\eta\eta x}) + \gamma\alpha^2 J(\Psi_{\eta\eta}, \Psi) - \mu\alpha\Lambda_\eta + B_x + \epsilon[B_X + \beta B_\eta] = 0 \quad (25)$$

$$\Lambda_t + \gamma U\Lambda_x + \gamma J(\Lambda, \Psi) + \alpha\Psi_\eta = 0 \quad (26)$$

$$B_t + \gamma U B_x + \gamma J(B, \Psi) - N_s^2(\Psi_x + \epsilon[\Psi_X + \beta\Psi_\eta]) = -\epsilon N_s^2\beta\sin t\,. \quad (27)$$

The Jacobian is now defined as $J(p, q){=}\alpha(p_xq_\eta{-}p_\eta q_x)$.

2.4 Vertical modes

At lowest order, we neglect all terms of order ϵ in (25)–(27), i.e. terms involving γ, δ or ϵ; this removes all the nonlinear and nonhydrostatic terms, as well as the barotropic forcing:

$$\alpha^2\Psi_{\eta\eta t} - \mu\alpha\Lambda_\eta + B_x = 0 \tag{28}$$

$$\Lambda_t + \alpha\Psi_\eta = 0 \tag{29}$$

$$B_t - N_s^2\Psi_x = 0\,. \tag{30}$$

Here the "slowly varying" topographic coordinate X enters the problem only via $\alpha{=}-1/h(X)$ and N_s, and acts at this order merely as a *parameter*, since there are no derivatives in X. Reducing the set to an equation for Ψ and assuming $\Psi{=}\phi(\eta, X)\exp i(kx{-}t)$ gives

$$\frac{\partial^2\phi}{\partial\eta^2} + \frac{k^2N_s^2}{\alpha^2(1-\mu)}\,\phi = 0\,. \tag{31}$$

Here k is a dimensionless wavenumber, depending parametrically on X. Together with the boundary conditions $\phi{=}0$ at $\eta{=}-1, 0$, this poses a Sturm-Liouville problem, whose solutions are given by orthogonal functions $\phi_n(\eta, X)$ with eigenvalues k_n. The structure of the eigenfunctions varies parametrically with X. Furthermore, the usual othogonality properties hold, i.e. for $n{\neq}m$

$$\int_{-1}^{0} d\eta\, N_s^2\phi_n\phi_m = 0\,. \tag{32}$$

For later usage, we define $c_n{=}(1{-}\mu)^{1/2}/k_n$, a dimensionless quantity, which in the rotationless case ($\mu{=}0$) can be interpreted as the phase speed. Via k_n, c_n depends on X, as one would expect since the phase speed depends on the local waterdepth and thus must vary with the topographic coordinate X.

2.5 Resulting model equations

We now reduce the higher-order set (25)–(27) by means of an expansion in the orthogonal eigenfunctions ϕ_n; thus, we write Ψ, B and Λ as

$$\Psi(t, x, X, \eta) = \sum_{n=1}^{n_{\max}} a_n(t, x, X)\phi_n(\eta, X) \tag{33}$$

$$\Lambda(t, x, X, \eta) = \sum_{n=1}^{n_{\max}} v_n(t, x, X)\phi_{n,\eta}(\eta, X) \tag{34}$$

$$B(t, x, X, \eta) = N_s^2(-\eta h(X))\sum_{n=1}^{n_{\max}} b_n(t, x, X)\phi_n(\eta, X)\,. \tag{35}$$

Since the resulting equations will be solved numerically, we anticipate a truncation at a certain modenumber $n_{\max}$. Notice that B is developed in terms of ϕ_n and hence vanishes at the bottom; this is in line with the assumption of a slowly varying topography. Over steep slopes, of course, a vanishing B would become unphysical; still, as we show in the following sections, the outcome of the model equations is overall satisfactory even in situations that mildly violate the restrictions imposed by the underlying assumptions.

We substitute (33)–(35) into (25)–(27), and multiply them by ϕ_k, $\phi_{k,\eta}$ and ϕ_k, respectively. Next we take the vertical integral and use the orthogonality properties of the modes.[1] This results in a set of coupled equations for the baroclinic modal coefficients a_k, v_k and b_k, representing the streamfunction, transverse velocity, and buoyancy, respectively:

$$a_{k,t} + \gamma U a_{k,x} - \delta c_k^2\sum_n L_{nk}a_{n,xxt}$$

$$+\gamma\alpha c_k^2\sum_{n,m} a_{n,x}a_m\Big\{\Big(\frac{1}{c_n^2} - \frac{1}{c_m^2}\Big)M_{mnk} - \frac{N_{mnk}}{c_m^2}\Big\}$$

$$-\frac{\mu}{\alpha}v_k - c_k^2[b_{k,x} + \epsilon b_{k,X}] - \epsilon c_k^2\sum_n b_n(R_{nk}{+}T_{nk}){=}0 \tag{36}$$

$$v_{k,t} + \gamma U v_{k,x} + \gamma\alpha c_k^2\sum_{n,m} a_m v_{n,x}\Big(\frac{M_{nmk}}{c_m^2} + \frac{M_{mnk}}{c_n^2}\Big) \tag{37}$$

$$-\gamma\alpha c_k^2\sum_{n,m} a_{n,x}v_m\Big(\frac{N_{mnk}{+}M_{nmk}{+}M_{mnk}}{c_m^2}\Big){+}\alpha a_k{=}0 \tag{38}$$

$$b_{k,t} + \gamma U b_{k,x}$$

$$+\gamma\alpha\sum_{n,m}\Big\{(a_m b_{n,x} - a_{n,x}b_m)M_{mnk} - a_{n,x}b_m N_{mnk}\Big\}$$

$$-[a_{k,x} + \epsilon a_{k,X}] - \epsilon\sum_n a_n(R_{nk} + T_{nk}) = -\epsilon D_k\sin t\,. \tag{39}$$

The coefficients denoted by capitals (L_{nk} etc.) stand for integral expressions, and are given in the appendix; note that they all depend on the topographic coordinate X.

One final simplification is to be made. In (36), the nonhydrostatic term (i.e. the term with δ) provides a coupling between modes. This is an undesirable effect, both from a physical and a numerical point of view (the set is solved much more efficiently if the coupling is absent). The underlying reason for the presence of this mode-coupling is as follows. We are using the modes derived from the hydrostatic limit (Sect. 2.4). Conveniently, in that case the vertical structure of the modes shows no dependence on the wave frequency. However, as we enter the nonhydrostatic regime, as in (36), a dependence on the wave frequency arises, leading to a modification of the modal structure, and this is precisely what the mode-coupling accomplishes. Note also that in the special case of constant stratification ($N_s{=}$const), the vertical structure never depends on the wave frequency, not even in the non-hydrostatic case; this is confirmed by the fact that L_{nk} vanishes for $n{\neq}k$ if $N_s{=}$const. For general N_s, the coupling terms can be removed by introducing explicitly a nonhydrostatic correction to the modes ϕ_n. This procedure was discussed in Appendix C of Gerkema (2001) and will not be

[1] Note that derivatives of N_s cancel when (35) is substituted into (25), since substitution in the terms $B_X{+}\beta B_\eta$ yields the combination $(N_s^2)_X{+}\beta(N_s^2)_\eta$, which is zero because of the dependence $N_s(-\eta h)$ and the definition of β.

repeated here. However, in the presence of Coriolis effects, the correction is not straightforward, and one actually needs to neglect terms of order $\delta\mu$ to solve the problem (the statement of the contrary in Gerkema (2001), namely that these terms would cancel automatically, is erroneous.) This formally necessitates assuming μ to be small as well. At the same time it is clear that (36) and (37) still contain the two Coriolis terms that were originally present in (6) and (7), so in that sense no approximation has been made.

Neglecting, then, L_{nk} for $n \neq k$, we arrive at the set of equations used hereafter; they contain the following effects:

- the forcing by the barotropic tidal flow over topography, represented by the term on the right-hand side of (39);
- barotropic advection, represented by $Ua_{k,x}$, and similarly for v_k and b_k;
- Coriolis effects; our assumption $\partial/\partial y=0$ implies that v is present merely as a result of Coriolis effects, and (37) would get decoupled from the rest if we take $\mu=0$;
- coupling terms due to *topography*, i.e. the terms with R and T;
- coupling terms due to *nonlinear interaction*, i.e. the terms involving M and N;
- nonhydrostatic effects, represented by the term with L_{kk} in (36).

Note that we did not impose any restriction on the *height* of the topography, so (36)–(39) can be used to model the generation of internal tides over the continental slope (examples are shown in the following sections). We have thus relaxed the assumption on (small) topography used in Gerkema (2001); still, the set of equations is just as easy to solve numerically, although there are of course some extra terms (topographic mode coupling, barotropic advection, horizontally varying coefficients α and c_k).

The set (36)–(39) is solved numerically using 4th-order centered differences in x and 3rd-order Adams-Bashforth in time (Durran, 1999); the presence of the nonhydrostatic term (with L_{kk}) leads to a tridiagonal matrix which is solved with the Thomas algorithm. We use a 4th-order spatial biharmonic filter to prevent instabilities on the grid scale. At the horizontal outer ends of the domain, we use sponge layers by including Rayleigh friction, whose thickness is 150 km and 50 km over the plain and the shelf, respectively (except in Sect. 3.1, where no sponge layers are used; here the domain was chosen large enough for the waves never to arrive at the boundaries). This suffices to absorb the incoming baroclinic waves and avoid reflection from the horizontal boundaries. The number of modes is specified below for each experiment, but we typically use between 10 and 30 modes. The numerical experiments show that the amplitude converges rapidly (the lowest modes being the most energetic), so that the beam is already well represented if one uses ten modes. We always start from a system at rest.

To facilitate the interpretation of the results in the oceanographic context, they will be presented in the figures in dimensional form, with the original horizontal coordinate being restored.

3 Solutions for linear hydrostatic case

We first look into the coupling between modes due to topography, and momentarily ignore the complicating factors of nonlinearity, nonhydrostaticity, and barotropic advection; thus we take $\gamma=\delta=0$, and (36)–(39) become

$$a_{k,t} - \frac{\mu}{\alpha} v_k - c_k^2[b_{k,x} + \epsilon b_{k,X}] - \epsilon c_k^2 \sum_n b_n(R_{nk}+T_{nk}) = 0 \quad (40)$$

$$v_{k,t} + \alpha a_k = 0 \quad (41)$$

$$b_{k,t} - [a_{k,x} + \epsilon a_{k,X}] - \epsilon \sum_n a_n(R_{nk} + T_{nk}) = -\epsilon D_k \sin t\,. \quad (42)$$

Despite the linear nature of this set, there are still terms representing mode-mode coupling, namely those with R and T; they are due to *topography*. They reflect the fact that separation of horizontal and vertical variables fails over the slope, implying that vertical modes cannot be regarded as mutually independent.

3.1 Inter-modal exchange of energy

In these experiments, we illustrate how topographically induced coupling engenders a transfer of energy between modes in a freely propagating depression that passes a seamount, given by a gaussian profile. Here we ignore the forcing term on the right-hand side of (42). The topography is supercritical and the stratification is taken constant. We first need to derive the expression of energy-density in terms of the modal coefficients; it can be obtained by returning to the original, scaled set (17)–(19), ignoring nonlinear and nonhydrostatic terms, and barotropic fields. After multiplication by $-\psi$, μv and b/N_s^2, respectively, adding up the resulting equations, and integrating over the vertical, we obtain the (dimensionless) energy equation

$$\frac{1}{2}\int dz \left\{(\psi_z)^2 + \mu v^2 + b^2/N_s^2\right\}_t - \int dz (b\psi)_x = 0\,. \quad (43)$$

(Here we used the fact that ψ vanishes at the boundaries.) This implies that the expression for energy density is

$$E = \frac{1}{2}\int dz \left\{(\psi_z)^2 + \mu v^2 + b^2/N_s^2\right\}.$$

Transformation to terrain following coordinates ($\eta=\alpha z$) turns it into

$$E = \frac{1}{2}\alpha^{-1}\int d\eta \left\{(\alpha\Psi_\eta)^2 + \mu\Lambda^2 + B^2/N_s^2\right\}.$$

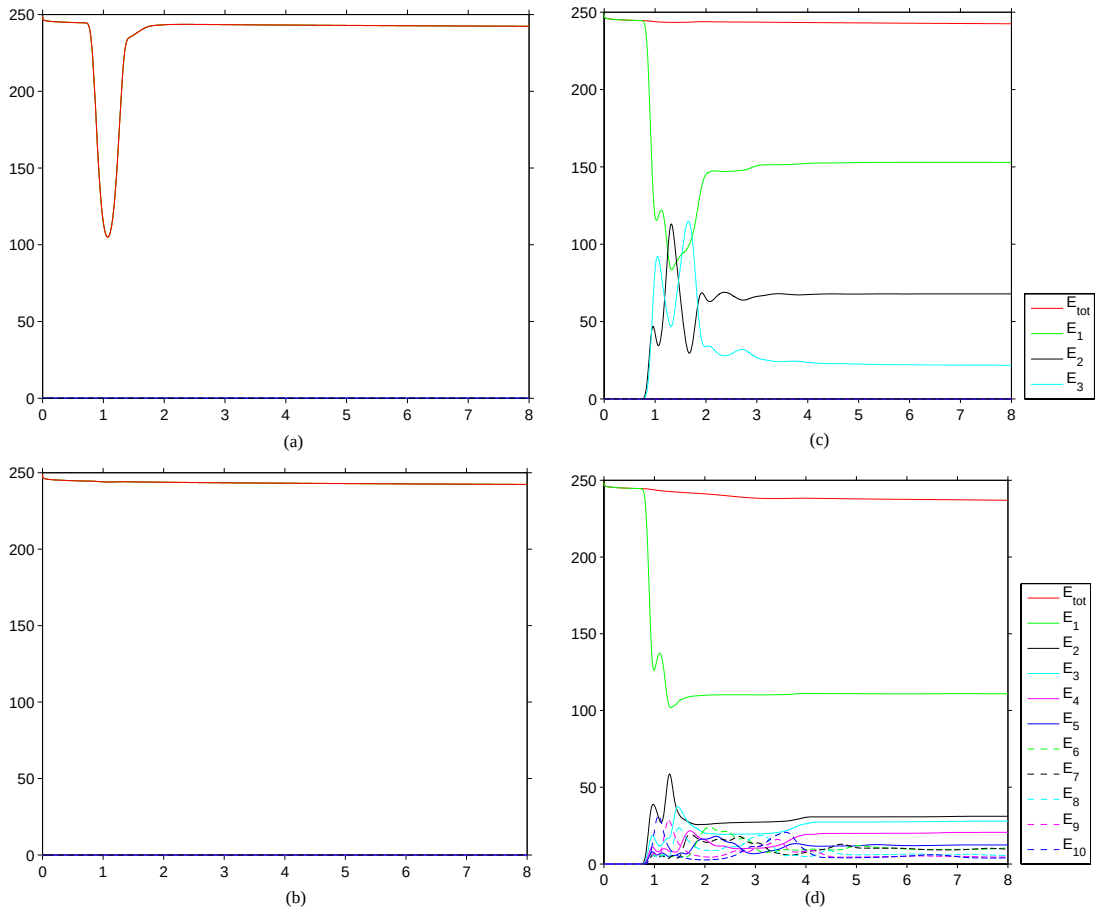

Fig. 1. The time-development of energy-density for one mode without interaction **(a)**, one mode with self-coupling **(b)**, three modes **(c)** and ten modes **(d)**. The red line represents the total energy.

Finally, substituting modes, (33)–(35), and using the orthogonality properties, gives

$$E = \frac{1}{2}\alpha^{-1}\sum_k F_k\left\{\frac{a_k^2}{c_k^2} + \mu\frac{v_k^2}{(\alpha c_k)^2} + b_k^2\right\}.$$

where $F_k = \int_{-1}^{0} d\eta\, N_s^2\phi_k^2$. This expression could also have been obtained directly from (40)–(42), but in that case there would have been no way of establishing the correct coefficient (F_k etc.). Also, the topographically induced interaction then thwarts an appropriate flux form; the terms with R and T seemingly act as a source or sink in the energy equation. This is merely a result of the transformation to terrain following coordinates. In the physically relevant system, i.e. in the original coordinates, no such sources/sinks are present, see (43). Indeed, from (43) it is clear that a transformation of the type $(\cdot)_x \to (\cdot)_x + \beta(\cdot)_\eta$ spoils the flux form since the coefficient β is not a constant but depends itself on η.

We study the development of a rightward propagating first-mode depression b_1, whose initial profile we prescribe along with $a_1 = -c_1\, b_1$ (with $u = \alpha\Psi_\eta$ in the transformed system). For these experiments, no sponge layers are used; the domain is chosen large enough to ensure that no wave reaches the boundary during the 8-period runs.

The results, shown in Fig. 1, clearly bring out the role of the topography in the interaction between modes. In fact, the interaction needs to be taken into account to avoid inconsistencies: in Fig. 1a, where all higher modes are excluded, the coupling terms are ignored, leading to a stark violation of conservation of energy as the depression passes the seamount. By contrast, in Fig. 1b (still for only the first mode), the (self-)coupling is included, and the energy is well conserved. The inclusion of higher modes engenders energy transfer from the first to higher modes as the depression moves over the seamount (Fig. 1c,d). The slight decrease of the total energy observed for ten modes is due to the biharmonic filter used to dampen oscillations on the grid scale. Its influence is stronger on the higher modes which have shorter wavelengths and which moreover stay longer over the shallow region (where the damping is stronger, for it includes the factor α). Notice also that the higher modes are subject to

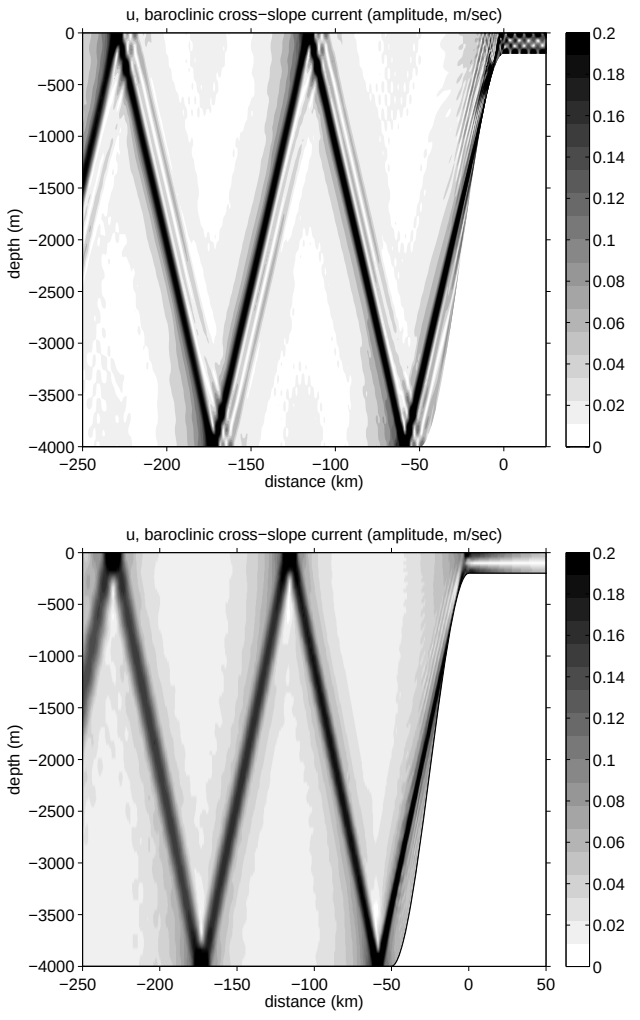

Fig. 2. Comparison of the amplitude of the cross-slope baroclinic velocity component (in $\mathrm{m\,s^{-1}}$) from the modal model for 30 modes at the 60th tidal period (upper panel) and a fully numerical model (lower panel). Both are linear and hydrostatic.

interaction over a longer period of time (as is clearly visible in Fig. 1d), because they propagate slower and therefore stay longer over the seamount. We emphasize that the "interaction" illustrated here is a purely linear process!

3.2 Comparison with fully numerical model

We now turn to the forced version of (40)–(42), and look at internal-tide generation over a continental slope. For this slope we use a cubic profile; its length is taken as 50 km, and the depths of the continental shelf and the abyssal plain are 200 m and 4000 m, respectively. The flux of the tidal forcing (M_2 frequency) is $Q{=}100\mathrm{m^2\,s^{-1}}$. Coriolis effects are here ignored. The stratification is uniform with $N{=}0.002\,\mathrm{s^{-1}}$. We present the results in terms of the baroclinic cross-slope current u, decomposed as follow:

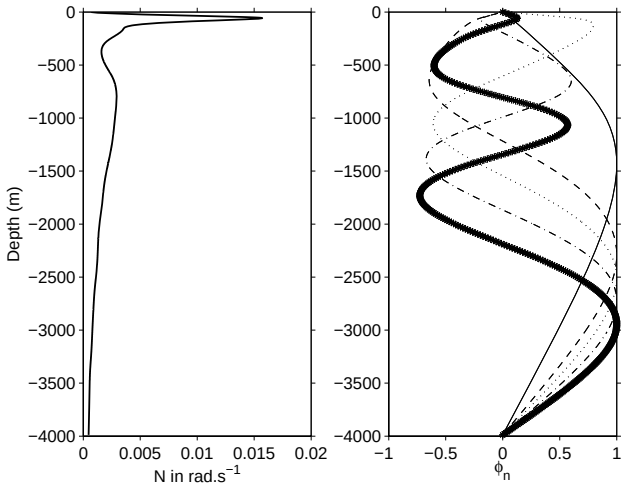

Fig. 3. Profile of the Brunt-Väisälä frequency N observed in the Bay of Biscay (left panel). First five baroclinic modes ϕ_n (right panel).

$$u(t,x,z) = A(x,z)\sin(\omega t - \Phi(x,z)) \tag{44}$$

where A and Φ are the amplitude and phase, respectively.

The internal tide manifests itself as a beam, propagating away from the shelf break (Fig. 2a). The beam has a slope that corresponds to the analytical expression for internal-wave characteristics, here in hydrostatic form: $s{=}(\omega^2{-}f^2)^{1/2}/N$. We compare the outcome of our modal model with that of a fully numerical internal-tide generation model, described by Gerkema et al. (2004), which too is linear and hydrostatic; the result from this model, for the same parameter values, is shown in Fig. 2b. We see that the angle of propagation as well as the intensity of the cross slope baroclinic current are in good agreement. This means that the modal model performs well even if the topographic scale is fairly short, since here it is even shorter than the internal-tide wavelength (the wavelength of the first mode being equal to the distance between two consecutive surface reflections of the beam). This confirms the expectation expressed in the Introduction, that the WKB-type derivation in practice remains valid well beyond its formal range of validity.

We now consider a more realistic setting, using observed stratification and topograpy profiles typical of the Bay of Biscay. This (summer) stratification is characterised by the presence of a strong seasonal thermocline at 60 m depth and a permanent pycnocline centered at 900 m depth (Fig. 3a). The vertical modes are derived from (31); their structure varies over the topography, via the dependence on X. The first five modes, over the plain, are shown in Fig. 3b.

In this experiment Coriolis effects are included ($f{=}1.070{\times}10^{-4}\,\mathrm{s^{-1}}$ at $47°10'$ N). The barotropic tidal forcing flux is $100\,\mathrm{m^2\,s^{-1}}$. The major generation region is located near the shelf break where the slope is critical, approximately at $z{=}{-}400$m, see Fig. 4a. The slope of

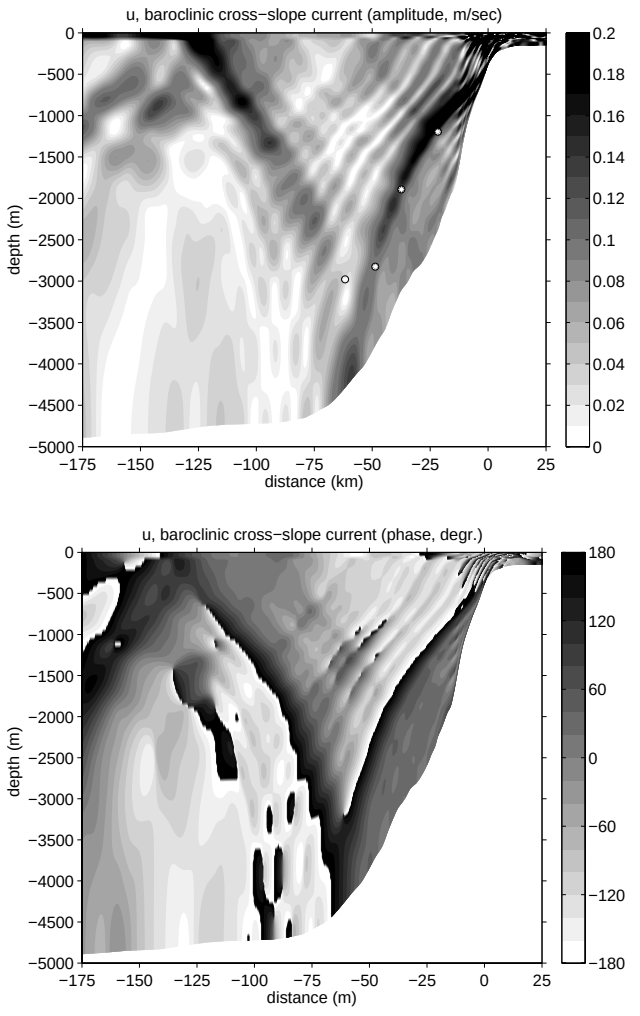

Fig. 4. The amplitude (in $\mathrm{m\,s^{-1}}$, upper panel) and phase (in degrees, lower panel) of the horizontal cross-slope baroclinic velocity component at the 30th tidal period for 10 modes. The white circles indicate the location of the downward and reflected beam observed by Pingree and New (1991).

the beam varies in the vertical because $N(z)$ varies. It is steeper in the weakly stratified abyss; here it reflects from the slope, and becomes wider and less intense as a result (defocusing). After this reflection, energy moves upward, and the beam finally meets the seasonal thermocline, near $x=-125\,\mathrm{km}$. Here it undergoes a severe distortion; the strong variation in N causes internal reflections, and gives rise to a quasi interfacial tide, visible by strong currents in the upper mixed layer. This mixture of beam-like and interfacial-like behaviour is typical for this stratification (Gerkema, 2001); the appearance of interfacial tides, during the passage of the beam through the seasonal thermocline, stands at the origin of the "local generation" of internal solitary waves, discussed below. The results from Fig. 4 are overall similar to those from a fully numerical model by Gerkema et al. (2004). Moreover, the path of the beam correponds well with the observations by Pingree and New (1991) (i.e. the depth of maximum excursions derived from CTD yoyoing), shown as circles in Fig. 4a.

4 Solutions for nonlinear nonhydrostatic case

We now consider the full set (36)–(39), thus including weakly nonlinear and nonhydrostatic effects. Nonlinearity has two principal effects on internal-tide propagation: the generation of higher harmonics during reflection from boundaries (due to interaction between incident and reflected beams), and the local generation of internal solitary waves. For the latter to happen, a seasonal thermocline is needed, but the former occurs already for constant stratification. We look into these effects in the next two sections.

4.1 Higher harmonics

The degree of nonlinearity depends on the strength of the barotropic tidal forcing. Figure 5 shows a snapshot of the cross-slope baroclinic current after 30 tidal periods for increasingly strong forcing. As in the earlier idealized experiment (Fig. 2), we use ten modes and have switched off rotation. Stratification is taken constant ($N{=}0.002\,\mathrm{s^{-1}}$). In panels *a* and *b*, the forcing is weak, and we are effectively in the linear regime. The transition toward the nonlinear regime is observed in panel *c*; here higher harmonics (i.e. waves at frequencies that are multiples of M_2) appear, faintly visible as steeper beams originating from the first bottom reflection. They are steeper because the steepness s of the beam, given by $s^2{=}(\omega^2{-}f^2)/(N^2{-}\omega^2)$, is a monotonically increasing function of ω. There is now a spatial redistribution of internal-tide energy, as is increasingly clear in subsequent panels.

To illustrate the appearance of higher harmonics more explicitly, we place three "moorings" over the abyssal plain, one before and two after the first bottom reflection. The energy spectrum for the cross-slope baroclinic current, averaged over total depth, shows a strong enhancement toward higher harmonics in the moorings after the point of reflection (Fig. 6a,b), compared to the mooring before reflection (Fig. 6c). This confirms the theoretical finding of generation of higher harmonics by nonlinear internal-wave reflection from boundaries (Tabaei et al., 2005; Gerkema, 2006).

4.2 Local generation of internal solitary waves

We now show model results in which a realistic configuration was chosen for topography and stratification. Our goal is to show that the scattering of the beam in the seasonal thermocline may produce internal solitary waves. For reasons of numerical stability, we choose an intermediate strength of the seasonal thermocline, typical of early June (Fig. 7), and a moderate tidal forcing ($Q{=}60\,\mathrm{m^2\,s^{-1}}$). In general, Coriolis

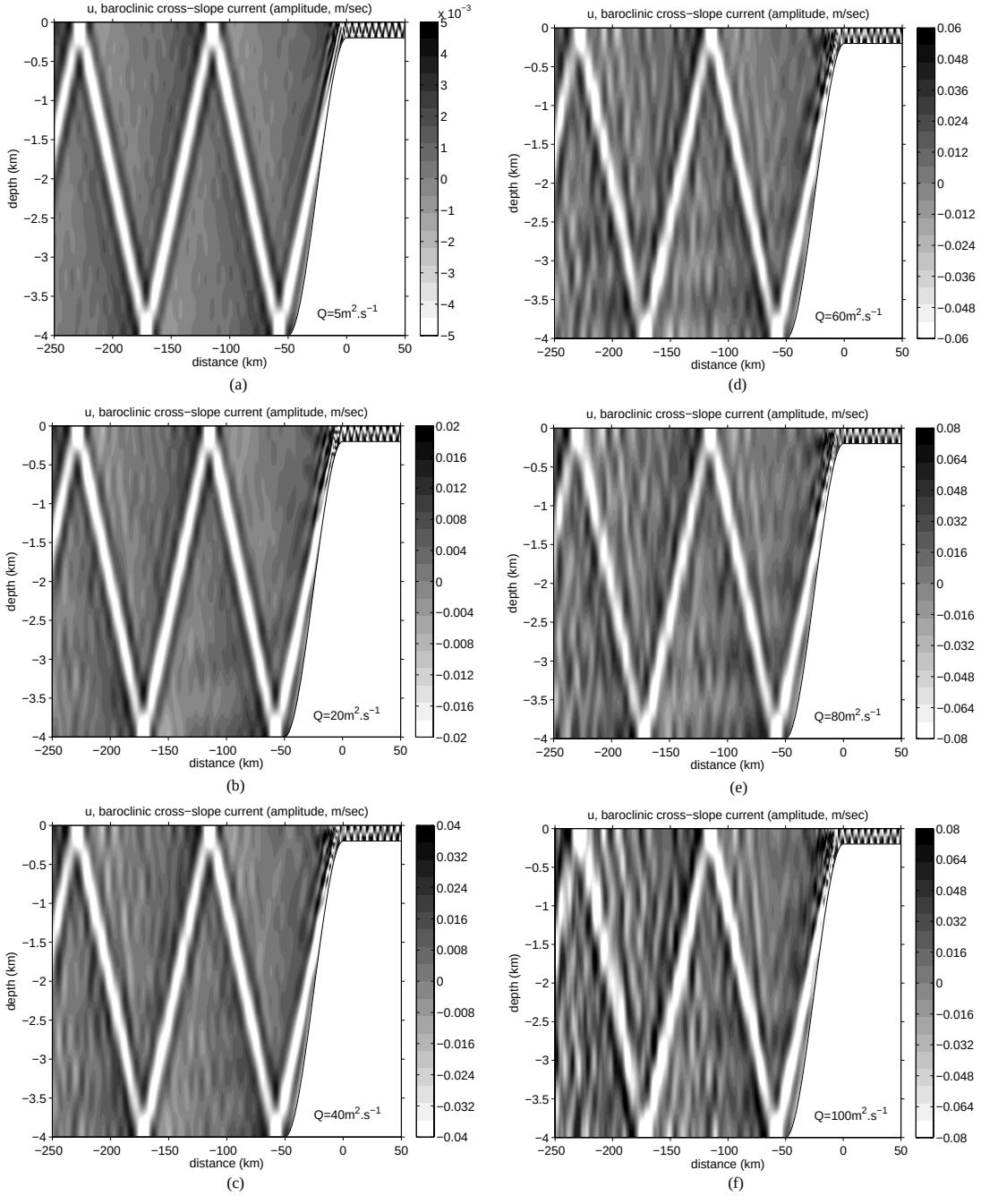

Fig. 5. Snapshot of the horizontal cross-slope baroclinic velocity component (in $\mathrm{m\,s^{-1}}$) for a barotropic tidal forcing increasing from 5 to $100\,\mathrm{m^2\,s^{-1}}$.

effects tend to suppress the generation of solitons (Grimshaw et al., 1998), and for this reason we exclude these effects here. It is understood that the suppressive effect by Coriolis dispersion could be compensated by an enhanced forcing, in which case internal solitary waves may still appear.

Figure 8 shows that there is an intense internal-wave activity near the thermocline in the immediate vicinity of the shelf break, which attenuates over the deep ocean. However, there is a resurgence of such activity over the abyssal plain, near $x=-100$ km, which is precisely at the point where the tidal beam encounters the seasonal thermocline. Here a depression forms, which gradually steepens and splits up into shorter peaks, the internal solitary waves. Their wavelength is about 2 km, which is consistent with the SAR imagery in

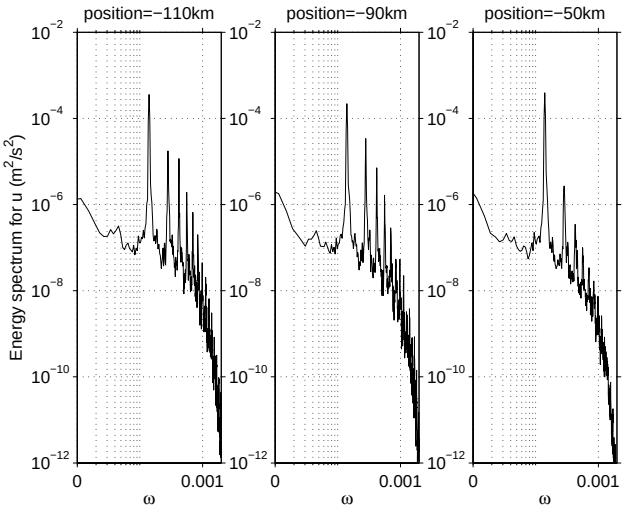

Fig. 6. Energy spectrum for the horizontal cross-slope baroclinic velocity component, averaged over total depth, at three different "moorings", before and after the reflection of the downward tidal beam: at −50 km (right panel), −90 km (middle panel), and −110 km (left panel).

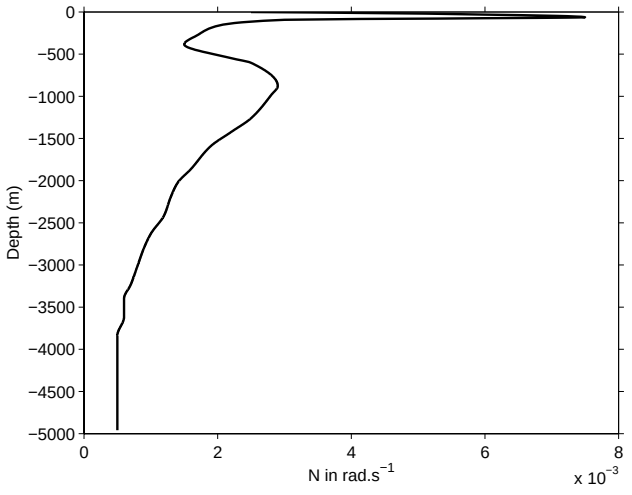

Fig. 7. The profile of N for the Bay of Biscay.

the Bay of Biscay (New and Da Silva, 2002) where the observed solitons have a wavelength between 0.9 and 2.7 km. This comparison is meaningful even though Coriolis dispersion was not included here, because Coriolis effects do not act significantly on the short solitary-wave lengthscale.

5 Discussion

The novel aspect of this paper is that we derived a coupled set of equations for the modal coefficients for weakly nonlinear nonhydrostatic internal-tide generation. We applied vertical modes despite the presence of a large-amplitude topography (continental slope), and this results in coupling terms between the modes over the slope which persist even if nonlinear term are neglected. In other words, there are two kinds of coupling in the model, one due to topography, the other due to nonlinear effects. Recently, Griffiths and Grimshaw (2007) derived a set of equations for internal-tide generation over large-amplitude topography, also using vertical modes. They did not assume a separation of length scales, and included all the topographically induced coupling terms. In this sense their model is exact, but they restricted themselves to the linear hydrostatic regime. The separation of scales we adopt here facilitates an ordering of small parameters and hence an extension to a weakly nonlinear nonhydrostatic regime.

A short discussion on the assumptions regarding the small parameters, and the range of validity thus imposed, is in order. Typical parameters (waterdepth $H = 4$km, internal-tide wavelength L=50 km, f=$1.0\times10^{-4}\,\mathrm{s}^{-1}$, wave frequency ω=$1.4\times10^{-4}\,\mathrm{s}^{-1}$, barotropic flux Q=$100\,\mathrm{m}^2\,\mathrm{s}^{-1}$) yield the following "small" parameters: γ=0.0036 (nonlinearity), δ=0.0064 (nonhydrostaticity), which are roughly of the same order of magnitude, as assumed in the derivation. For solitary waves, which are much shorter than the internal tide, say a few km, the parameter δ would seem to be of order one, violating the initial assumptions. However, since solitary waves are trapped at the thermocline, a more appropriate measure of waterdepth becomes the thickness of the mixed layer h_1, as is seen for example in the expression for the linear phase speed, $(g'h_1)^{1/2}$. Still, the derivation presented here fits in the KdV framework and thus supposes both upper and lower layers to be "shallow". For realistic parameters, a different approach (e.g. like in the Benjamin-Ono equation) may seem necessary, but it is a fact of experience that the KdV equation often outperformes alternative equations even when the parameter regime suggests the latter to be more appropriate (e.g., Koop and Butler, 1981). Regarding Coriolis effects, we do not suppose the parameter μ to be of the order of γ; indeed, the two Coriolis terms are fully present in (36)–(37), so in that sense no smallness of μ is assumed. It is only in the eliminiation of the mode-coupling due to nonhydrostatic effects (see Sect. 2.5) that μ has to be assumed to be small. However, nonhydrostatic effects become important only at short scales, and at these scales Coriolis effects are automatically weak (this could be formally expressed by introducing a second frequency, $\hat{\omega}$, appropriate for the short scales, with $\hat{\omega}\gg\omega$, yielding a small $\hat{\mu}$). In short, no real restriction on μ is imposed. Finally, we assume the topography to be slowly varying, as expressed by the smallness of ϵ. This is, at face value, a questionable assumption, but, as noted in the Introduction, the practical range of validity of WKB-like assumptions often stretches far beyond the formal limitations.

This is confirmed by a comparison with more sophisticated numerical models, which shows that the formal assumption of "slowly varying" topography does not in practice pose serious restrictions (Sect. 3b). In the nonlinear, nonhydrostatic regime, we showed that higher harmonics are generated, similar to what fully numerical models (like MIT-gcm) showed before (Gerkema et al., 2006). Compared to these models, the present model is less exact as it involves a few approximations; on the other hand, it is computationally much less demanding than fully nonhydrostatic models, and is conceptually linked to the Korteweg-deVries type soliton equations. (We note that numerical instabilities occur for strong forcing, possibly requiring a modification of the numerical scheme in that case.) As we showed in Sect. 4b, the model can be used to describe the process of local generation of internal solitary waves by an internal-tide beam impinging on the seasonal thermocline. This phenomenon has been observed in the Bay of Biscay (New and Pingree, 1990, 1992; New and Da Silva, 2002), and some theoretical studies have been devoted to it (Gerkema, 2001; Akylas et al., 2006). However, the latter studies adopted a somewhat idealized setting, and we think the results in Sect. 4b show the phenomenon for the first time in a model based on a realistic setting of topography, stratification, and tidal forcing.

Appendix A Integral expressions

The evolution equations for the modal coefficients (36)–(39) contain the following integral expressions, serving as coefficients. First, the topographically induced mode-coupling:

$$R_{nk} = \frac{\int_{-1}^{0} N_s^2 \phi_{n,X} \phi_k d\eta}{\int_{-1}^{0} N_s^2 \phi_k^2 d\eta} \tag{A1}$$

$$T_{nk} = \frac{\int_{-1}^{0} \beta N_s^2 \phi_{n,\eta} \phi_k d\eta}{\int_{-1}^{0} N_s^2 \phi_k^2 d\eta} . \tag{A2}$$

Second, the one associated with the barotropic tidal forcing term:

$$D_k = \frac{\int_{-1}^{0} \beta N_s^2 \phi_k d\eta}{\int_{-1}^{0} N_s^2 \phi_k^2 d\eta} . \tag{A3}$$

Third, the nonlinear terms

$$M_{mnk} = \frac{\int_{-1}^{0} N_s^2 \phi_{m,\eta} \phi_n \phi_k d\eta}{\int_{-1}^{0} N_s^2 \phi_k^2 d\eta} \tag{A4}$$

$$N_{mnk} = \frac{\int_{-1}^{0} (N_s^2)_\eta \phi_m \phi_n \phi_k d\eta}{\int_{-1}^{0} N_s^2 \phi_k^2 d\eta} . \tag{A5}$$

(Note that the latter vanishes for constant stratification.) Finally, the nonhydrostatic term

$$L_{nk} = \frac{\int_{-1}^{0} \phi_n \phi_k d\eta}{\int_{-1}^{0} N_s^2 \phi_k^2 d\eta} . \tag{A6}$$

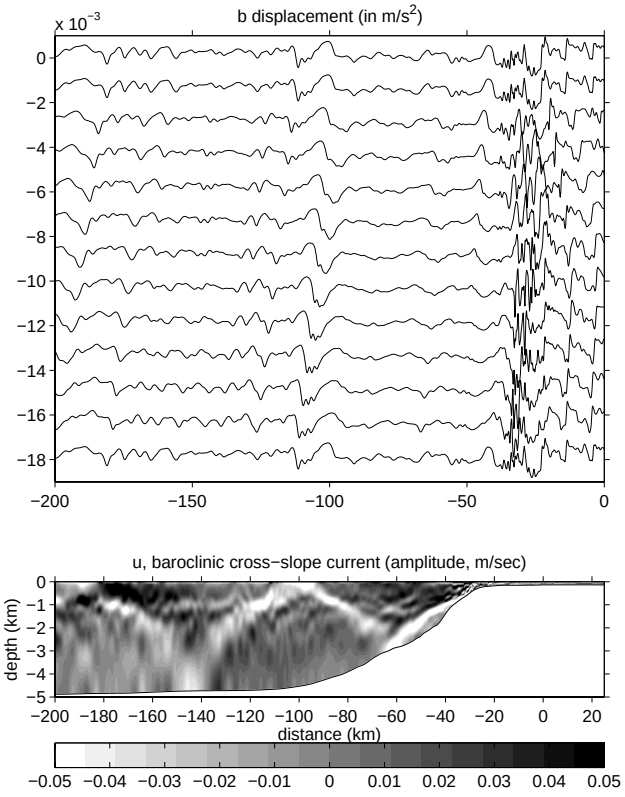

Fig. 8. Elevation of the interface (represented by minus buoyancy b) at 50 m for each tidal hour (time progresses by steps of 1/12 tidal period), and the amplitude (in $\mathrm{m\,s^{-1}}$) of the horizontal cross-slope baroclinic velocity component.

Acknowledgements. The authors are grateful to A. Colin de Verdière and A. Pichon for discussions and comments on an earlier version of this work, as part of a PhD thesis (Maugé, 2006). Detailed comments from two reviewers greatly helped us to improve the manuscript. R. Maugé was financially supported by EPSHOM-UBO contract 02 87 060 00 470 29 25, and TG by NWO/ALW program CLIMA-DIM.

Edited by: R. Grimshaw
Reviewed by: three anonymous referees

References

Akylas, T. R., Grimshaw, R. H. J., Clarke, S. R., and Tabaei, A.: Reflecting tidal wave beams and local generation of solitary waves in the ocean thermocline, J. Fluid Mech., 593, 297–313, 2007.

Bender, C. M. and Orszag, S. A.: Advanced mathematical methods for scientists and engineers, McGraw-Hill, 1978.

Durran, D. R.: Numerical methods for wave equations in geophysical fluid dynamics, Springer, 1999.

Garrett, C. and Gerkema, T.: On the body-force term in internal-tide generation, J. Phys. Oceanogr., 37, 2172–2175, 2007.

Gerkema, T.: Internal and interfacial tides: beam scattering and local generation of solitary waves, J. Mar. Res., 59, 227–255,

2001.

Gerkema, T., Internal-wave reflection from uniform slopes: higher harmonics and Coriolis effects, Nonlin. Processes Geophys., 13, 265–273, 2006, http://www.nonlin-processes-geophys.net/13/265/2006/.

Gerkema, T., Lam, F. P. A., and Maas, L. R. M.: Internal tides in the Bay of Biscay: conversion rates and seasonal effects, Deep-Sea Res. II, 51(25/26), 2995–3008, 2004.

Gerkema, T., Staquet, C., and Bouruet-Aubertot, P.: Decay of semi-diurnal internal-tide beams due to subharmonic resonance, Geophys. Res. Lett., 33, L08604, doi:10.1029/2005GL0250105, 2006.

Griffiths, S. D. and Grimshaw, R. H. J.: Internal tide generation at the continental shelf modelled using a modal decomposition: two-dimensional results, J. Phys. Oceanogr., 37, 428–451, 2007.

Grimshaw, R. H. J., Ostrovsky, L. A., Shrira, V. I., and Stepanyants, Y. A.: Long nonlinear surface and internal gravity waves in a rotating ocean, Surv. Geophys., 19, 289–338, 1998.

Helfrich, K. R. and Melville, W. K.: Long nonlinear internal waves, Annu. Rev. Fluid Mech., 38, 395–425, 2006.

Khatiwala, S.: Generation of internal tides in an ocean of finite depth: analytical and numerical calculations, Deep-Sea Res. I, 50, 3–21, 2003.

Koop, C. G. and Butler, G.: An investigation of internal solitary waves in a two-fluid system, J. Fluid Mech., 112, 225–251, 1981.

Lamb, K. G.: Numerical experiments of internal wave generation by strong tidal flow across a finite amplitude bank edge, J. Geophys. Res., 99, 843–864, 1994.

Maugé, R.: Modèles de génération des marées internes, Université de Bretagne Occidentale, Brest, PhD-thesis, 2006.

New, A. L. and Da Silva, J. C. B.: Remote-sensing evidence for the local generation of internal soliton packets in the Central Bay of Biscay, Deep-Sea Res., 49, 915–934, 2002.

New, A. L. and Pingree, R. D.: Large-amplitude internal soliton packets in the central Bay of Biscay, Deep-Sea Res., 37, 513–524, 1990.

New, A. L. and Pingree, R. D.: Local generation of internal soliton packets in the central Bay of Biscay, Deep-Sea Res., 39, 1521–1534, 1992.

Pingree, R. D. and New, A. L.: Abyssal penetration and bottom reflection of internal tidal energy into the Bay of Biscay, J. Phys. Oceanogr., 21, 28–39, 1991.

Tabaei, A., Akylas, T. R., and Lamb, K. G.: Nonlinear effects in reflecting and colliding internal wave beams, J. Fluid Mech., 526, 217–243, 2005.

Vlasenko, V. I. and Morozov, E. G.: Generation of semidiurnal internal waves near a submarine ridge, Oceanology, 33, 282–286, 1993.